Chapter 3

High-contrast dielectric metasurfaces

Metamaterials are artificially structured media composed of subwavelength constituents, called metaatoms, that enable extraordinary manipulation of all types of waves. Specifically, in this context, the shaping of electromagnetic waves, or light. At visible and near-infrared wavelengths (400–1000 nm), the most popular choice for beam shaping is the two-dimensional version of metamaterials, called metasurfaces. For high-contrast dielectric metasurfaces, a dielectric medium is patterned with a flat, two-dimensional lattice of metaatoms that can impart a designed phase profile to an incident beam, shaping its wavefront [121]. This chapter begins by detailing how the refraction of light can be arbitrarily steered by a phase profile at the interface between two media [40], and how the manipulation of this gradient enables the shaping of virtually any beam. The conventional approach to metasurface design, known as phase mapping, is then discussed alongside the implications of the standard metaatom geometries. A limitation of this phase-mapping approach is the limited spatial sampling, which degrades efficiency when deflecting light at steep angles or constructing a metasurface with large numerical aperture (NA). To address this limited sampling, the chapter introduces an alternative approach with diffractive superunit cells for beam shaping at large angles. Finally, the chapter outlines the computational methods used to simulate individual metaatoms and approximate the full beam shaping, concluding with the fabrication processes and free-space transmission experiments.

3.1 Beam shaping with dielectric metasurfaces

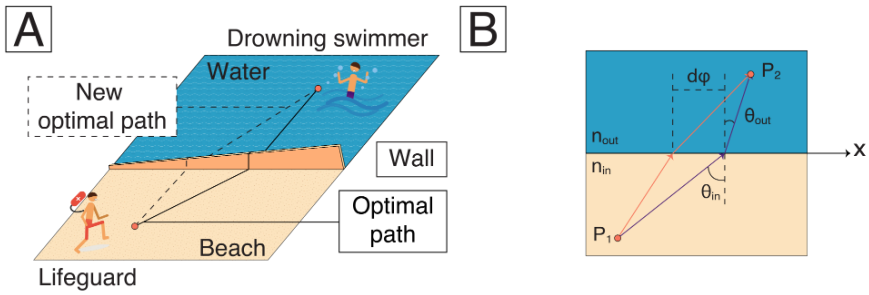

Figure 3.1: A) A wall with a varying height along the interface between the beach and water changes the optimal path for the lifeguard to save a drowning swimmer. This is analogous to how the refraction of light can be controlled via a designed phase-gradient ($\frac{\mathrm{d}\phi}{\mathrm{d}x}$), represented by the wall with a varying height in the lifeguard analogy. **B)** Geometry to derive generalized Snell's law of refraction with Fermat's theorem.

As introduced in chapter one, classical refractive optics, such as the lenses in your glasses, shape the phase profile of a beam through transversely varying phase accumulation from propagating through a shaped piece of a higher-refractive-index medium, such as glass. In contrast, a metasurface is a nanostructure at an interface designed to impose a transversely varying phase profile onto an incident beam via scattering from subwavelength metaatoms. It was mathematically formalized as a generalization of Snell's law in 2011 [40], showing that the refraction of a beam can be arbitrarily steered by a phase-gradient along an interface between two media. Introducing a phase-gradient ($\frac{\mathrm{d}\phi}{\mathrm{d}x}$) at an interface generalizes the refraction from Snell's law as

$$n_{\text{out}} \sin\theta_{\text{out}} - n_{\text{in}} \sin\theta_{\text{in}} = \frac{\lambda_0}{2\pi} \frac{\mathrm{d}\phi}{\mathrm{d}x}, \tag{3.1}$$

where n_{in} and n_{out} denote the refractive indices of the respective media, and θ_{in} and θ_{out} are the angles of incidence and refraction. **Figure 3.1A** illustrates an analogy for the generalized Snell's law by extending the classic high-school problem to derive Snell's law via Fermat's principle. Fermat's principle states that light always takes the path that can be traveled in the least time, which is equivalent to saying it follows the trajectory that minimizes the accumulated phase of the wave. In the analogy, a lifeguard seeks the optimal path

to rescue a drowning swimmer, taking into account that running on the beach is significantly faster than swimming in the water. For the analogy to work, the lifeguard is also extremely proficient at his job because he always chooses the optimal path to save the drowning swimmer.

To extend the analogy to generalized Snell's law, an additional obstacle is introduced: the lifeguard must also account for the time required to climb a wall of varying height along the shoreline, between the beach and the water. By changing the height of this wall along the shoreline, it is possible to manipulate the optimal path for the lifeguard, from any starting position, to any position of the drowning swimmer. The phase profile ($\frac{\mathrm{d}\phi}{\mathrm{d}x}$) in the generalized Snell's law is analogous to a wall with varying height, but for light. Furthermore, **Eq. 3.1** can be formally derived, just as in high school, by applying Fermat's principle and trigonometry to an interface that imparts a transversely varying phase-gradient ($\frac{\mathrm{d}\phi}{\mathrm{d}x}$), as depicted in **Fig. 3.1B** [40]. The same treatment can be applied to the reflected wave to acquire the generalized Snell's law of reflection.

The implication of **Eq. 3.1** is that, by designing a transverse variation of the phase gradient along an interface, any phase profile can be imposed on an incident beam, which can shape the transmitted wavefront[1]. Furthermore, since electromagnetic waves are periodic with 2π, shifting the phase by 2π returns the wave to its original state. Therefore, the designed phase gradient ($\frac{\mathrm{d}\phi}{\mathrm{d}x}$) of the metasurface only needs to span 0–2π to achieve arbitrary beam shaping, referred to as full-phase coverage.

Choosing a desired phase profile is the starting point for constructing a metasurface, from which the phase gradient is inferred. This is typically done by either replicating a phase profile from a refractive optical element or using a numerically computed profile to target an arbitrary beam shape. Three examples of phase profiles of refractive optical components that are used throughout the thesis are the lens, the blazed grating, and

[1]However, it is argued that this form of generalized Snell's law (**Eq. 3.1**) is in reality only valid under certain conditions, such as for a linear phase gradient [122]. But, as with the two-level system, it is a great starting point for explaining the beam-shaping function of the metasurface.

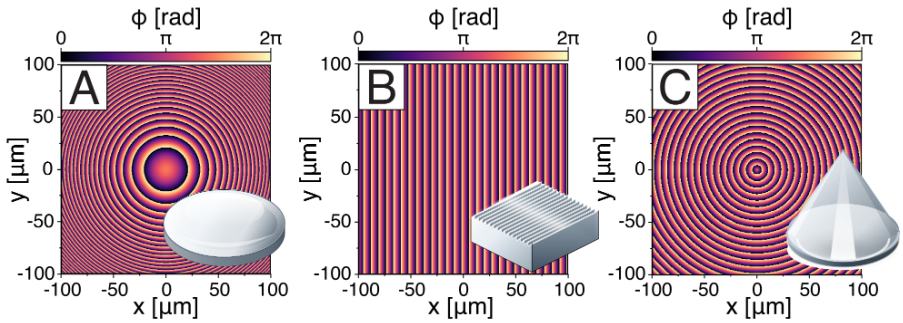

Figure 3.2: Examples of the transverse phase profiles for three refractive optical components with illustrations of the shaped pieces of glass with the corresponding phase profiles. **A)** The hyperbolic phase profile for collimation or focusing of light, with focal length f. **B)** The linear phase profile of a blazed grating that can deflect light by the angles Θ_x and Θ_y. **C)** The conical phase profile of an axicon for generating counter-propagating beams, where NA is the numerical aperture of the axicon.

an axicon

$$\begin{aligned} \phi_{\text{lens}} &= -\frac{2\pi n_{\text{out}}}{\lambda_0}\left(\sqrt{x^2+y^2-f^2}-f\right), \\ \phi_{\text{blazed}} &= -\frac{2\pi n_{\text{out}}}{\lambda_0}\left(x\sin\Theta_x + y\sin\Theta_y\right), \\ \phi_{\text{axicon}} &= -\frac{2\pi n_{\text{out}}}{\lambda_0}\text{NA}\sqrt{x^2+y^2}, \end{aligned} \tag{3.2}$$

where n_{out} is the refractive index of the medium the light is transmitted to. The three profiles are illustrated in **Fig. 3.2**, where the hyperbolic phase profile of a lens is used to focus or collimate light (f), and the linear phase profile of the blazed grating that deflects light to a certain angle (Θ_x and Θ_y). The axicon will generate counter-propagating waves that form a Bessel beam if the beam is incident on the middle of the axicon [92]. An advantage of metasurfaces is that combining the phase profiles of multiple elements corresponds to a linear operation. This means that the functionality of several cascaded optical components can be multiplexed into a metasurface with a single layer of metaatoms.

To instead target an arbitrary beam shape with a metasurface, it is possible to obtain the required phase profile by starting from an arbitrary desired shape at a certain distance from the metasurface. The beam can then be numerically backpropagated to the metasurface plane

to compute the phase profile that produced the beam. This is a widely used methodology for projecting holograms [64]. To efficiently compute the phase profiles, the Gerchberg–Saxton algorithm is commonly used, where the optical field is iteratively propagated back and forth between the target image plane and the metasurface plane until the required phase profile converges [123].

3.2 Phase mapped metasurface

The conventional way to implement the phase profile with a metasurface is called *phase mapping*. In this approach, the phase profile is discretized into a subwavelength periodic lattice, yielding a matrix of local phase shifts that an individual metaatom should impart. To acquire these local phase shifts, the metasurface is treated as a thin optical component layer at an interface that imparts an amplitude and phase to an incident field ($\mathbf{E}_{\text{in}}$), which produces the transmitted field ($\mathbf{E}_{\text{out}}$), as illustrated in **Fig. 3.3A**. The general response of the metasurface can, in this way, be mathematically formulated as a transversely dependent Jones matrix ($\mathbf{J}(x, y)$) as

$$\mathbf{E}_{\text{out}}(x, y) = \mathbf{J}(x, y)\mathbf{E}_{\text{in}}(x, y) = \begin{bmatrix} j_{xx}(x, y) & j_{xy}(x, y) \\ j_{yx}(x, y) & j_{yy}(x, y) \end{bmatrix} \mathbf{E}_{\text{in}}(x, y), \quad (3.3)$$

where $j = |j|e^{i\phi}$ are complex transmission coefficients. By restricting the individual metaatoms to be birefringent waveplates with orthogonal optical axes, rotated by an in-plane angle θ, the continuous Jones matrix ($\mathbf{J}(x, y)$) can be discretized in the linear polarization basis as

$$\mathbf{J}(x, y) \approx \sum_{p,q} \hat{\mathbf{J}}_{(p,q)} = \sum_{p,q} \mathbf{R}\left[-\theta_{(p,q)}\right] \begin{bmatrix} \hat{j}_{x,(p,q)} & 0 \\ 0 & \hat{j}_{y,(p,q)} \end{bmatrix} \mathbf{R}\left[\theta_{(p,q)}\right]. \quad (3.4)$$

Here, the matrix $\hat{\mathbf{J}}_{(p,q)}$ represents the local, discrete optical response (denoted by the hat) for a metaatom at the position indexed by (p, q) in the two-dimensional lattice. The matrix $\hat{\mathbf{J}}_{(p,q)}$ contains all the discrete transmission coefficients $\hat{j}_{x,(p,q)}$ and $\hat{j}_{y,(p,q)}$ and the in-plane rotation $\mathbf{R}\left[\theta_{(p,q)}\right]$ for the different birefringent metaatoms of the metasurface.

A discretized periodic lattice of metaatoms is exemplified in **Fig. 3.3B** by a square lattice with the lattice constant a. Metaatoms are, however,

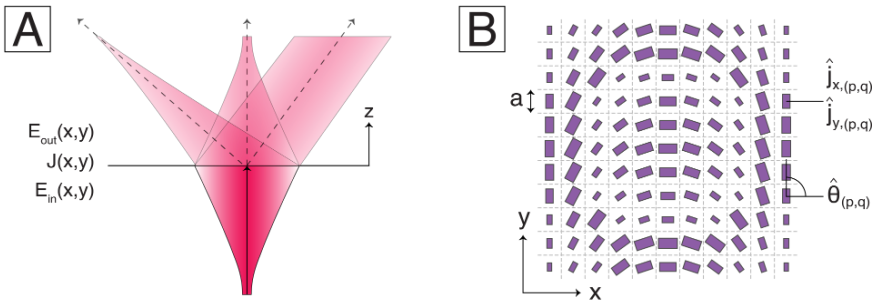

Figure 3.3: A) The metasurface can be modeled as a thin optical component. By altering the Jones matrix ($\mathbf{J}(x, y)$) for a certain incident beam ($\mathbf{E}_{\text{in}}$), it is possible to shape it into (almost) any transmitted beam ($\mathbf{E}_{\text{out}}$). **B)** A desired phase profile can be approximated by discretization of a Jones matrix ($\hat{\mathbf{J}}_{(p,q)}$) with the desired phase profile on a square subwavelength lattice (lattice constant a). Here, $\hat{j}_{x,(p,q)}$ and $\hat{j}_{x,(p,q)}$ is the complex transmission of the metaatom at index (p, q) and rotated by the in-plane rotation $\mathbf{R}\left[\hat{\theta}_{(p,q)}\right]$.

not limited to only a birefringent half-waveplate with two orthogonal optical axes, as in **Eq. 3.4** [124]. Several computational methods and inverse design algorithms generate complex, freeform metaatom geometries for efficient metasurface design or extended functionalities [125–127]. Nevertheless, restricting the analysis of metaatom geometry to **Eq. 3.4** greatly simplifies the analytical analysis of the implications of the metaatom geometry.

In this phase-mapping approach, the discrete metaatoms are assumed to have a constant phase across the unit cell. This implies that the ideal phase profile is approximated by sampling at discrete constant-phase levels spanning 0–2π. This sampling is exemplified in **Fig. 3.4A** with the hyperbolic phase profile of a lens (**Eq. 3.2**). Furthermore, when discretizing the metasurface into a periodic lattice, the lattice itself can impart an in-plane wave vector and diffract the incident beam ($\mathbf{E}_{\text{in}}$). The lattice constant (a) can be chosen such that all higher diffraction orders can be suppressed, thus only transmitting a beam ($\mathbf{E}_{\text{out}}$) by the zeroth order. In **Fig. 3.4B**, a periodic lattice is shown when illuminated by an incident field ($\mathbf{E}_{\text{in}}$), together with the corresponding wave vectors of the incident (k_{in}), transmitted (k_{out}), and reflected field (k_{ref}) fields. The condition for suppressing the diffraction orders in a square lattice is obtained by considering the possible in-plane wave vector ($\frac{2\pi m}{a}$) that

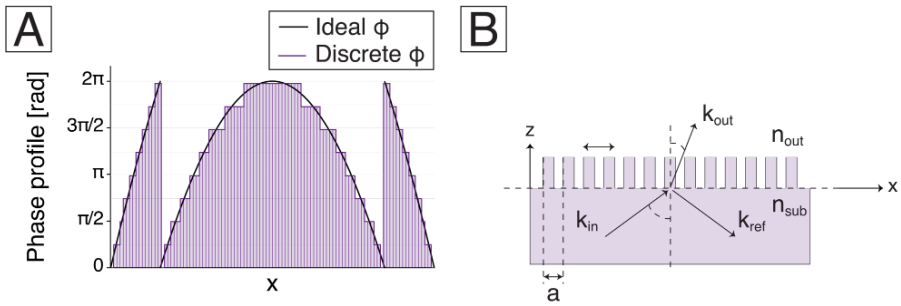

Figure 3.4: **A)** The ideal phase profile when discretized by sampling the phase profile with eight different metaatoms, imparting eight discrete phase shifts spanning 0–2π. **B)** All higher orders of diffraction are suppressed when the periodic lattice of the metasurface has a lattice constant that is smaller than the wavelength in the substrate.

can be added by the lattice and the dispersion relations for either media,

$$\begin{aligned} k_{x,\text{in}} + \frac{2\pi}{a}m = k_{x,\text{out}}, \quad k^2 = k_z^2 + k_x^2 \rightarrow \quad a < \lambda_0, \\ k_{x,\text{in}} + \frac{2\pi}{a}m = k_{x,\text{ref}}, \quad k^2 = k_z^2 + k_x^2 \rightarrow \quad a < \frac{\lambda_0}{n_{\text{sub}}}, \end{aligned} \tag{3.5}$$

where m is an integer denoting the diffraction order. When these conditions are satisfied, the propagation constant, k_z, becomes imaginary for all higher diffraction orders ($m \neq 0$) in both transmission and reflection. This means they correspond to an evanescent wave in the propagating direction, which decays exponentially and does not transport energy into the far field. Thus, by limiting the lattice constant to be smaller than the wavelength in the substrate ($\frac{\lambda_0}{n_{\text{sub}}}$), all higher-order diffraction is suppressed in both transmission and reflection.

3.2.1 Dynamic phase metasurfaces

The most straightforward metasurfaces are called dynamic phase (or propagation phase), where the dimensions of a specific geometry, for example, a rectangular cuboid, as shown in **Fig. 3.5A**, are varied to achieve the local phase shifts. The dynamic phase metasurface can simultaneously impart two independent phase profiles ($\hat{\phi_x}$ and $\hat{\phi_y}$) onto either linear polarization state along the optical axis of the birefringent waveplate metaatom. If the geometry of the metaatom is varied but not

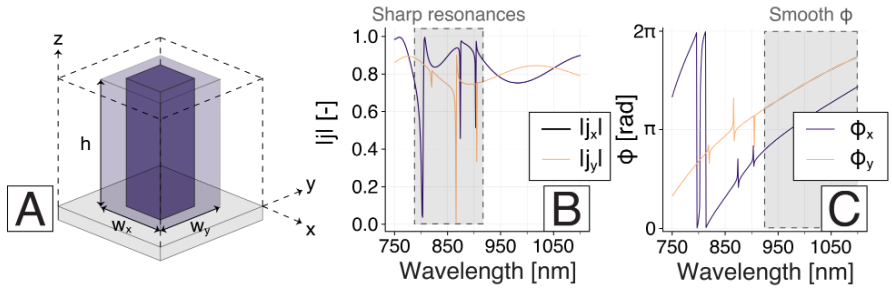

Figure 3.5: A) An example of a metaatom for a dynamic phase metasurface is a rectangular cuboid, where the height (h) and widths (w_y and w_x) can be varied to impart different phases and transmissions. **B)** The transmission spectrum ($|\hat{j_x}|$ and $|\hat{j_x}|$) for either optical axis of the rectangular cuboid. **C)** The corresponding phase spectrum (ϕ_x and ϕ_y) for either optical axis of the rectangular cuboid.

rotated ($\theta = 0$), the local response of the metaatom (**Eq. 3.4**) for a field in a linear polarization basis is

$$\hat{\mathbf{J}}_{\text{dynamic}}\mathbf{E}_{\text{lin}} = \begin{bmatrix} \hat{j}_x & 0 \\ 0 & \hat{j}_y \end{bmatrix} \begin{bmatrix} E_x \\ E_y \end{bmatrix} = \hat{x}|\hat{j}_x|e^{i\hat{\phi}_x}E_x + \hat{y}|\hat{j}_y|e^{i\hat{\phi}_x}E_y. \tag{3.6}$$

Here, the decoupled transmission coefficients imply the statement above: the dynamic-phase metaatom can simultaneously impart two independent phase profiles ($\hat{\phi}_x$ and $\hat{\phi}_y$), one for each linear polarization state along either optical axis of the metaatom. Furthermore, a metaatom geometry without birefringence ($\hat{j}_x = \hat{j}_y$), such as a cylinder, will sacrifice the ability to impart independent phase profiles in favor of being polarization-insensitive.

The local phase delays produced by dynamic-phase metaatoms are often explained phenomenologically as a change in the effective refractive index, where a larger metaatom simply increases the local index relative to the surrounding medium, resulting in a greater phase delay. This perspective is inaccurate because the electromagnetic field is not uniformly distributed across the metaatom unit cell, and it conceptually reduces the metasurface to a fancier diffractive optical element. A more accurate description is that the high-contrast metaatoms are discrete scatterers that can strongly confine the electric field, supporting localized electromagnetic resonances such as Mie and geometric resonances [50, 128]. As

seen in the transmission spectrum in **Fig. 3.5B**, the cuboid supports several resonances in the wavelength range 750–950 nm[2]. However, when designing metaatoms for a dynamic-phase metasurface, it is desirable to operate far from these sharp resonances, in a region where the phase delay changes gradually, as shown in **Fig. 3.5C**, because this relaxes the fabrication tolerances of the metaatoms.

3.2.2 Resonant phase metasurface

While metaatoms in dynamic-phase metasurfaces are typically designed to operate far away from a resonance peak in wavelength, resonant-phase metasurfaces instead utilize them directly. As with the dynamic-phase approach, the dimensions of metaatoms with fixed geometry are varied to achieve the desired optical response, with the distinction that operation now relies directly on tuning these geometric resonances [129]. The transmittance and reflectance of electric and magnetic Mie-type resonances, approximated as Lorentzian resonances, can be analytically expressed as

$$\begin{aligned} \hat{j}_{\text{resonant}} &= 1 + \frac{2i\gamma_e\omega}{\omega_e^2 - \omega^2 - 2i\gamma_e\omega} + \frac{2i\gamma_m\omega}{\omega_m^2 - \omega^2 - 2i\gamma_m\omega}, \\ \hat{r}_{\text{resonant}} &= \frac{2i\gamma_e\omega}{\omega_e^2 - \omega^2 - 2i\gamma_e\omega} - \frac{2i\gamma_m\omega}{\omega_m^2 - \omega^2 - 2i\gamma_m\omega}, \end{aligned} \tag{3.7}$$

where γ_e and γ_m are the damping coefficients for the electric- and magnetic-induced dipoles, respectively, and ω_e and ω_m are their corresponding resonant angular frequencies [130]. By tuning the physical dimensions of the Mie particle, it is possible to overlap these resonances ($\omega_e = \omega_m$) while perfectly matching their damping coefficients ($\gamma_e = \gamma_m$). This creates perfect destructive interference for the reflection, yielding unity transmission, known as the Kerker condition [131]. Because the analytical expressions above only apply to spherical Mie particles and the dipole approximation, finding the Kerker condition in more practical geometries typically requires a numerical scheme. While the Kerker condition allows the resonant-phase metasurface to achieve theoretically unity transmission, its resonant nature makes the metasurface sensitive to perturbations, yielding low fabrication tolerances and a narrow operating bandwidth. However, this high sensitivity also makes it a promising platform for active, tunable metasurfaces, such as changing the state of

[2]For the simulation of the spectrum, the cuboid and the substrate have the refractive index $n = 3.52$ and are sitting in an air environment

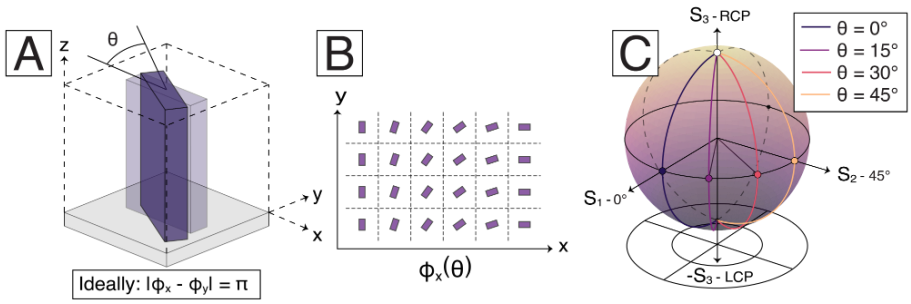

Figure 3.6: **A)** The birefringent metaatom utilized for a geometric phase metasurface, called a nanofin, where the in-plane rotation angle (θ) is used to impart the designed phase profile. **B)** By rotating the nanofins across the metasurface, a phase profile is imparted via the geometric phase. **C)** The Poincaré sphere when mapped with four different trajectories of an RCP state that is transformed to an LCP state via a half-waveplate nanofin at four different in-plane rotation angles (θ). The RCP state is at the north pole of the sphere, which is transformed to the LCP state at the south pole. However, the trajectory to the LCP state depends on the in-plane rotation of the nanofin, which is how the geometric-phase phenomenon is visualized.

phase-change media [132], applying thermal tuning [133], or infiltrating with liquid crystals [134, 135].

3.2.3 Geometric phase metasurfaces

The Pancharatnam-Berry (PB) metasurface, or geometric phase metasurface, is named after its discovery in classical optics by Pancharatnam [136] and its generalization to quantum systems by Berry [137]. The geometric phase is a surprising (or unintuitive) phase shift that appears from the transformation of the polarization state of a field. Pancharatnam found that the geometric phase shift between two states is exactly half the solid angle of the closed loops formed by the transformation trajectories when mapped onto the Poincaré sphere, hence the name geometric phase. While this geometrical description is somewhat dense, the geometric phase in the context of a birefringent metaatom can be seen mathematically with Jones calculus.

For geometric-phase metasurfaces, the birefringent metaatoms are typically referred to as nanofins. To design a metasurface with a phase profile based on the geometric phase, the geometric-phase shift is mapped to a

local, in-plane rotation (θ) of a nanofin, depicted in **Fig. 3.6A**. Because the local phase delay will vary with in-plane rotation (θ), the geometric-phase metasurface is typically constructed from nanofins of the same dimensions, rotated across the metasurface to create a phase profile via the geometric phase, as illustrated in **Fig. 3.6B**. The geometric phase due to the in-plane rotation (θ) is acquired by expanding the Jones matrix for the birefringent metaatom (**Eq. 3.4**) as

$$\begin{aligned}\hat{\mathbf{J}}_{\mathrm{pb}}(\theta) &= \mathbf{R}(-\theta)\begin{bmatrix}\hat{j}_x & 0\\ 0 & \hat{j}_y\end{bmatrix}\mathbf{R}(\theta)\\ \hat{\mathbf{J}}_{\mathrm{pb}}(\theta) &= \begin{bmatrix}\hat{j}_x\cos^2\theta + \hat{j}_y\sin^2\theta & \left(\hat{j}_x - \hat{j}_y\right)\sin\theta\cos\theta\\ \left(\hat{j}_x - \hat{j}_y\right)\sin\theta\cos\theta & \hat{j}_x\sin^2\theta + \hat{j}_y\cos^2\theta\end{bmatrix}.\end{aligned} \tag{3.8}$$

By defining two complex transmission coefficients, one for the light that will have a transform polarization state and acquire the geometric phase $\left(\hat{j}_{\mathrm{pb}} = \frac{\hat{j}_x - \hat{j}_y}{2}\right)$, and one for the untransformed light $\left(\hat{j}_0 = \frac{\hat{j}_x + \hat{j}_y}{2}\right)$, the above equation can be simplified as

$$\hat{\mathbf{J}}_{\mathrm{pb}}(\theta) = \hat{j}_0\begin{bmatrix}1 & 0\\ 0 & 1\end{bmatrix} + \hat{j}_{\mathrm{pb}}\begin{bmatrix}\cos 2\theta & \sin 2\theta\\ \sin 2\theta & -\cos 2\theta\end{bmatrix}. \tag{3.9}$$

Because of the identity matrix in the first term, this component retains its original polarization state. Because the geometric phase requires a polarization transformation, the first term is independent of the in-plane rotation angle (θ) of the nanofin and does not acquire the geometric phase.

The ideal nanofin for a geometric phase metasurface is a half-wave plate since the coefficient for the untransformed light ($\hat{j}_0$) can be completely canceled. With the nanofin as a half-waveplate with equal transmittance along both optical axes

$$\phi_y - \phi_x = \pi, \quad |\hat{j}_x| = |\hat{j}_y| = |\hat{j}|, \tag{3.10}$$

the coefficients for the transformed and untransformed light are simplified as

$$\hat{j}_0 = \frac{|\hat{j}|}{2}e^{i\phi_x}\left(1 + e^{i(\phi_y - \phi_x)}\right) = \frac{|\hat{j}|}{2}e^{i\phi_x}\left(1 + e^{i\pi}\right) = \frac{|\hat{j}|}{2}e^{i\phi_x}(1 - 1) = 0 \tag{3.11}$$

and

$$\hat{j}_{\mathrm{pb}} = \frac{|\hat{j}|e^{i\phi_x} - |\hat{j}|e^{i\phi_y}}{2} = |\hat{j}|e^{i\phi_x} = |\hat{j}|. \tag{3.12}$$

where the phase shift $e^{i\phi_x}$ in the final expression can be omitted since both the polarization state and phase profile are invariant under a common phase shift. Thus, the coefficient for the untransformed light ($\hat{j}_0$) is completely canceled, and all light will undergo the polarization transformation above and acquire a geometric phase.

By illuminating the half-waveplate nanofin with a right-hand circularly polarized beam (RCP [3]) it can now be seen how the nanofin converts the RCP state and imparts the geometric phase from the in-plane rotation

$$\begin{aligned}\hat{\mathbf{J}}_{\mathrm{pb}}(\theta)\hat{r} &= \frac{\hat{j}_{\mathrm{pb}}}{\sqrt{2}}\left[\hat{x}(\cos 2\theta - i\sin 2\theta) + \hat{y}(\sin 2\theta + i\cos 2\theta)\right] \\ &= \hat{j}_{\mathrm{pb}}e^{-2i\theta}\left(\frac{\hat{x} + i\hat{y}}{\sqrt{2}}\right) \\ &= \hat{j}_{\mathrm{pb}}e^{-2i\theta}\hat{l}.\end{aligned} \tag{3.13}$$

This phase shift of 2θ is known as the geometric phase. Furthermore, the RCP state is transformed to a left-handed circularly polarized (LCP) state, the conjugate state on the opposite side of the Poincaré sphere. In **Fig. 3.6C**, the Poincaré sphere illustrates four different trajectories for an RCP state transformed by a half-wave plate nanofin oriented at four different in-plane angles ($\theta = 0°, 15°, 30°, 45°$). This visualization allows us to directly test Pancharatnam's geometric statement. The closed loop formed by the trajectories for $\theta = 0°$ and $\theta = 45°$ encloses a quarter of the surface of the sphere, as seen in **Fig. 3.6C**. A quarter of a sphere has a solid angle of π, which then corresponds to a geometric phase shift of $\pi/2$ or 90°. This matches the result from our Jones calculus (**Eq. 3.13**), where the relative geometric phase between the two nanofins is twice the in-plane rotation (2θ), meaning that the rotation of a nanofin by 45° results in a relative geometric phase shift of 90°.

However, a consequence of the geometric phase[4] can be seen by instead

[3] The circular polarization basis vectors $\hat{r} = \frac{1}{\sqrt{2}}\begin{bmatrix}1\\-i\end{bmatrix}$ and $\hat{l} = \frac{1}{\sqrt{2}}\begin{bmatrix}1\\i\end{bmatrix}$

[4] And a limitation for when the intended light source is linearly polarized. An example of a linearly polarized light source is a VCSEL.

illuminating the same nanofin with a linearly polarized beam

$$\begin{aligned}\hat{\mathbf{j}}_{\mathrm{pb}}(\theta)\hat{x} &= \hat{j}_{\mathrm{pb}} \begin{bmatrix}\cos 2\theta \\ \sin 2\theta\end{bmatrix} \\ &= \hat{j}_{\mathrm{pb}} \left(\hat{x}\cos 2\theta + \hat{y}\sin 2\theta\right) \\ &= \frac{\hat{j}_{\mathrm{pb}}}{\sqrt{2}} \left(\left(\hat{r}+\hat{l}\right)\cos 2\theta + i\left(\hat{r}-\hat{l}\right)\sin 2\theta\right) \\ &= \frac{\hat{j}_{\mathrm{pb}}}{\sqrt{2}} \left(\hat{r}e^{2i\theta} + \hat{l}e^{-2i\theta}\right).\end{aligned} \tag{3.14}$$

Thus, the geometric phase (2θ) is acquired by both the circular polarization states, but with opposite signs. This means the linearly polarized beam is split into its RCP and LCP constituents, each acquiring the same phase profile but with opposite signs. Therefore, in practice, a geometric-phase metasurface can be designed for only one handedness of light at a time. For example, designing a convex, focusing lens for RCP imposes the phase profile of a concave, divergent lens on the LCP part of the beam.

There is a resilience to fabrication tolerance with geometric-phase metasurfaces compared to dynamic-phase or resonant-phase metasurfaces. Since the designed phase profile is due to the in-plane rotation angle (θ) of the nanofin, the precision of the approximation of the phase profile is determined by the precision of the lithography equipment rather than the etching process. If the etch depth or geometry is slightly wrong and the nanofin does not form a perfect half-waveplate, it theoretically does not distort the designed phase profile. It will result in a larger fraction of the incident beam remaining in its original polarization state ($\hat{j}_0$) and passing through the metasurface without acquiring the geometric phase. But the fraction of light that picks up the geometric phase ($\hat{j}_{\mathrm{PB}}$) will, however, still experience a geometric phase profile as determined by the rotation of the nanofins. In contrast, if the metaatoms of a dynamic phase metasurface are not etched to the correct depth, the metasurface phase profile becomes distorted and impairs beam shaping.

3.2.4 Arbitrary polarization metasurfaces

As seen in the previous sections, the dynamic and geometric phase metasurfaces operate either in the linear or the circular polarization basis. However, it is possible to combine the two concepts to impart two

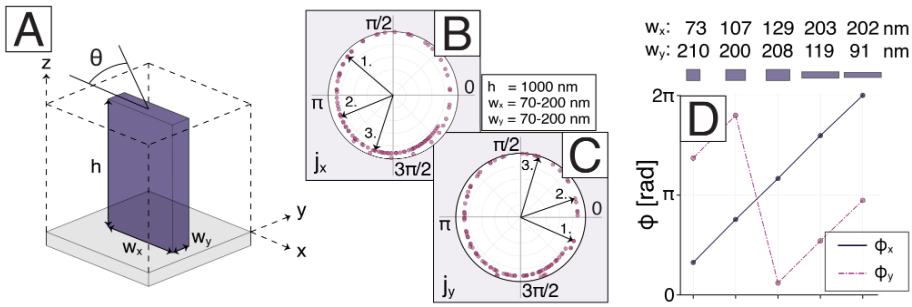

Figure 3.7: **A)** A birefringent waveplate that can be used to construct an APM by varying its dimensions (w_x, w_y, and h) and its rotation (θ). **B)** The transmission coefficients ($\hat{j}_x$ and $\hat{j}_y$) along either of the optical axes of a GaAs metaatom with a fixed height ($h = 1000$ nm) while sweeping the widths of the metaatom (w_x and w_y). The arrows mark three metaatoms with a phase difference of π between the optical axes, making them half-waveplates. **C)** Five selected metaatoms that are half-waveplates ($|\phi_x - \phi_y| = \pi$), but with varying dynamic-phase delays along either optical axis (ϕ_x and ϕ_y). These half-waveplate metaatoms can be used to design a metasurface to impart two independent phase profiles to the RCP and LCP states of an incident beam.

independent phase profiles onto two arbitrary, orthogonal polarization states. This functionality was first demonstrated for dielectric metasurfaces in 2015 [138], and later mathematically formalized [139]. This type of metasurface will be referred to here as an arbitrary polarization metasurface (APM), although the concept often appears under the name spin-decoupled metasurface [73, 140–142].

To acquire the Jones matrix ($\hat{\mathbf{J}}_{\text{apm}}$) for an APM, it is assumed that the metasurface can impart two independent phases ($e^{i\phi_+}$ and $e^{i\phi_-}$, with unity transmission), onto two orthogonal polarization states of an incident beam (λ^+ and λ^-) and in the process transforming the beam into the two new orthogonal polarization states (κ^+ and κ^-) as

$$\begin{aligned} \hat{\mathbf{J}}_{\text{apm}}\lambda^+ &= e^{i\phi_+}\kappa^+, \\ \hat{\mathbf{J}}_{\text{apm}}\lambda^- &= e^{i\phi_-}\kappa^-. \end{aligned} \tag{3.15}$$

While the transmitted polarization states (κ^+ and κ^-) can theoretically be any arbitrary states, restricting the metasurface to a single layer of birefringent metaatoms, as seen in **Fig. 3.7A**, constrains $\hat{\mathbf{J}}_{\text{apm}}$ to the symmetric form seen earlier for the geometric-phase metasurface (**Eq. 3.4**). It can be generally shown that a single birefringent waveplate

will always transform the polarization state to the conjugate state [139], implying

$$\kappa^{+} = \overline{\lambda^{+}}, \quad \kappa^{-} = \overline{\lambda^{-}}, \tag{3.16}$$

where the overline denotes the complex conjugate. (An example of this was seen with the geometric-phase nanofin that transformed the RCP state into the conjugate LCP state in **Eq. 3.13**). Under the constraint from **Eq. 3.16**, the system of equations in **Eq. 3.15** can be simultaneously solved to compute the required Jones matrix as

$$\hat{\mathbf{J}}_{\text{apm}} = \begin{bmatrix} e^{i\phi_+}\overline{\lambda_1^+} & e^{i\phi_-}\overline{\lambda_1^-} \\ e^{i\phi_+}\overline{\lambda_2^+} & e^{i\phi_-}\overline{\lambda_2^-} \end{bmatrix} \begin{bmatrix} \lambda_1^+ & \lambda_1^- \\ \lambda_2^+ & \lambda_2^- \end{bmatrix}^{-1}. \tag{3.17}$$

By evaluating **Eq. 3.17** for a pair of orthogonal polarization states with two desired phase profiles, one obtains the required spatial Jones matrix ($\hat{\mathbf{J}}_{\text{apm}}$), which can then be spatially discretized as described before. The required transmission coefficients can be found by parametrically sweeping the dimensions of the birefringent metaatoms. In **Fig. 3.7B**, a parametric sweep of the transmission coefficients in the linear polarization basis is presented for the GaAs metaatom in **Fig. 3.7A**, with a fixed height ($h = 1000$ nm) and varying widths (w_x and w_y). By identifying metaatoms that are half-waveplates ($|\phi_x - \phi_y| = \pi$), it is possible to construct an APM that imparts two independent phase profiles onto the circular polarization basis (RCP and LCP). The three marked metaatoms in **Fig. 3.7B** are such half-waveplates, since they have a phase-delay difference of π between their optical axes. Furthermore, **Fig. 3.7C** illustrates the difference in the dynamic phase (ϕ_x and ϕ_y) for either optical axis of five half-waveplate metaatoms. The functionality of imparting an independent phase profile onto the RCP and LCP states with an APM with the metaatoms in **Fig. 3.7C** is used later in the thesis.

To gain further physical insight into the APM, it is instructive to evaluate the matrix $\hat{\mathbf{J}}_{\text{apm}}$ using the circular polarization basis, defined as

$$\lambda_{+} = \begin{bmatrix} 1 \\ -i \end{bmatrix}, \quad \lambda_{-} = \begin{bmatrix} 1 \\ i \end{bmatrix}. \tag{3.18}$$

Using these states in **Eq. 3.17** yields the matrix in the form

$$\hat{\mathbf{J}}_{\text{apm}} = \frac{1}{2} \begin{bmatrix} e^{i\phi_+} + e^{i\phi_-} & i\left(e^{i\phi_+} - e^{i\phi_-}\right) \\ i\left(e^{i\phi_+} - e^{i\phi_-}\right) & -\left(e^{i\phi_+} + e^{i\phi_-}\right) \end{bmatrix}. \tag{3.19}$$

This matrix can be diagonalized, resulting in the eigenvalues

$$\lambda_1 = e^{i\phi_1} = e^{\frac{i}{2}(\phi_+ + \phi_-)}, \quad \lambda_2 = e^{i\phi_2} = e^{\frac{i}{2}(\phi_+ + \phi_-) - i\pi}, \tag{3.20}$$

and eigenvectors

$$\mathbf{V} = \begin{bmatrix} \mathbf{V}_1 & \mathbf{V}_2 \end{bmatrix} = \begin{bmatrix} \cos\theta & -\sin\theta \\ \sin\theta & \cos\theta \end{bmatrix}, \quad \theta = \frac{1}{4}\left(\phi_- - \phi_+\right), \tag{3.21}$$

allowing us to express the Jones matrix in the diagonalized form as

$$\hat{\mathbf{J}}_{\text{apm}} = \begin{bmatrix} \cos\theta & -\sin\theta \\ \sin\theta & \cos\theta \end{bmatrix} \begin{bmatrix} e^{i\phi_1} & 0 \\ 0 & e^{i\phi_2} \end{bmatrix} \begin{bmatrix} \cos\theta & \sin\theta \\ -\sin\theta & \cos\theta \end{bmatrix}, \tag{3.22}$$

which takes the exact form of a rotated birefringent waveplate from **Eq. 3.4**.

In addition, in the circular-polarization basis, the geometric and dynamic phases are decoupled, providing explicit instructions for designing an APM. First, the π phase difference between the two eigenvalues

$$\phi_1 - \phi_2 = \pi. \tag{3.23}$$

implies that the birefringent metaatom acts as a half-wave plate[5]. Secondly, as seen in **Eq. 3.22**, the eigenvalues of the metaatom correspond to a dynamic phase shift along the optical axes of the metaatom

$$\lambda_1 = e^{i\phi_1} = e^{\frac{i}{2}(\phi_+ + \phi_-)} \quad \rightarrow \quad \phi_1 = \frac{\phi_+ + \phi_-}{2}. \tag{3.24}$$

And finally, the geometric phase is encoded by the in-plane rotation of the half-wave plate (**Eq. 3.21**) of the metaatom

$$\theta = \frac{\phi_- - \phi_+}{4}. \tag{3.25}$$

By rearranging these two relationships for ϕ_1 and θ, a linear system of equations is found that links the desired phase profiles (ϕ_+ and ϕ_-) to the geometric and dynamic phase as

$$\begin{cases} \phi_+ &= \phi_1 - 2\theta \\ \phi_- &= \phi_1 + 2\theta \end{cases}. \tag{3.26}$$

[5]Which might have been expected the previous section and the choice of working in the circular polarization basis.

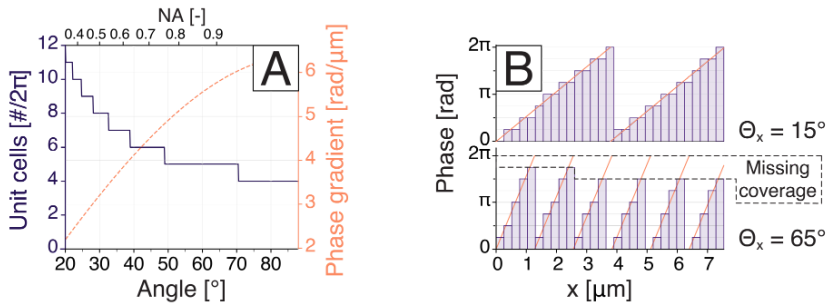

Figure 3.8: A) The number of unit cells (a = 260 nm) that can fit within one periodicity of a blazed grating (linear phase profile) as a function of the deflection angle and the corresponding NA. **B)** A linear phase profile discretized into eight equal steps on a subwavelength lattice with periodicity of 260 nm. At a smaller deflection angle ($\Theta_x = 15°$), the full range is properly sampled, but for a steeper deflection angle ($\Theta_x = 65°$), a certain range of the phase profile is missing coverage with the discrete metaatoms.

This means that both RCP and LCP acquire a dynamic phase from the corresponding eigenvalue of the metaatom. The in-plane rotation imparts a geometric phase, and as before, the LCP and RCP states will experience phase profiles with opposite signs. However, because the dynamic and geometric phases are decoupled (**Eq. 3.26**), two independent phase profiles can be created for each of the circular polarization states.

3.3 Beam shaping with superunit cell metasurfaces

With the conventional phase-mapped metasurface, the lattice constant is commonly made subwavelength to suppress higher diffraction orders (**Eq. 3.5**). One drawback is the limited sampling rate of the phase profile, set by the lattice constant (a). In **Fig. 3.8A**, the number of unit cells per 2π periodicity is shown for a square lattice (a = 260 nm) as a function of a blazed grating (linear phase profile) needed for deflection to a certain angle. Furthermore, the actual phase-gradient ($\frac{d\phi}{dx}$) is shown as a function of the blazed grating (linear phase profile) needed for deflection to the same deflection angle. The approximation of the phase profile by the metaatoms becomes progressively worse as a steeper or more rapidly changing phase profile is needed. As exemplified in **Fig. 3.8B**, where a linear phase profile for deflection of light to a

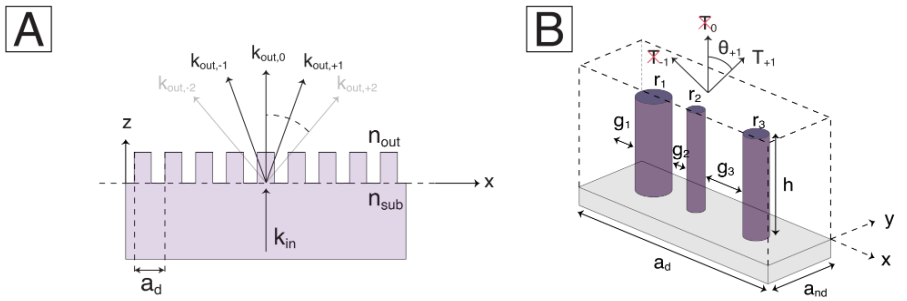

Figure 3.9: A) A periodic lattice (a_d) with the wave vectors for an incident beam (k_in) and the transmitted higher order of diffraction ($k_{\mathrm{out},m}$). **B)** The metaatoms within one superunit cell will impart a phase and amplitude to each of the open diffraction orders. By arranging the relative position ($g_1,\ g_2,\ g_3$), radii ($r_1,\ r_2,\ r_3$) and the height (h) of the metaatoms, destructive interference can be achieved in all but one diffraction order (T_{+1}). This deflects the incident light to an angle set by the diffractive period of the superunit cell (a_d).

smaller angle ($\Theta_x = 15°$) and a steeper angle ($\Theta_x = 65°$) is discretized by eight constant-phase metaatoms with the same lattice constant ($a = 260$ nm). For a smaller deflection angle, fourteen metaatoms fit within one period of the phase profile, which allows them to cover the full 0–2π range. However, at the steeper angle, only five metaatoms fit within one period, leaving part of the phase profile with missing coverage. Therefore, the conventional phase-mapping approach is limited in resolving steep phase gradients, or rapidly changing phase profiles, which are required, for example, to deflect light at large angles or to fabricate lenses with very large NA.

An alternative is the *superunit cell* metasurface [143,144]. In contrast to the phase-mapping approach, this metasurface uses a superunit cell that acts as a local diffractive grating. This creates a local linear phase profile, or deflection angle, across the superunit cell, compared to the constant phase across the unit cells in the phase-mapping approach. To accomplish this, the superunit cell periodicity exceeds the wavelength in one dimension, labeled as the diffractive periodicity (a_d). This intentionally allows (opens) higher diffraction orders. In **Fig. 3.9A**, a periodic lattice with lattice constant a_d can be seen with the corresponding wave vectors for an incident beam and the higher diffraction orders, similarly to **Fig. 3.4B**. The diffraction orders that correspond to propagating waves are determined by the wave vector imparted by the square lattice ($\frac{2\pi m}{a_\mathrm{d}}$)

and the dispersion relation as

$$k_{x,\mathrm{in}} + \frac{2\pi}{a_\mathrm{d}} m = k_{x,\mathrm{out}}, \quad k^2 = k_z^2 + k_x^2 \quad \rightarrow \quad a_\mathrm{d} > \lambda_0 m. \tag{3.27}$$

When this condition is met, the m-th diffraction order corresponds to a propagating wave. Similarly, the larger periodicity opens diffraction orders for the reflected beam as well $\left(a_\mathrm{d} > \frac{\lambda_0}{n_\mathrm{sub}} m\right)$. The lattice constant for the other dimension of the superunit cell is typically set to be smaller than the substrate wavelength to suppress higher diffraction orders, as discussed before, and is labeled the non-diffractive periodicity (a_nd).

Within this larger superunit cell, several different metaatoms can now be placed, each with a certain amplitude and a phase contribution to each diffraction order. By tuning the dimensions and positions of the metaatoms in the superunit cell, it is possible to control the constructive and destructive interference for each of the diffraction orders. Crucially, it is possible to create an arrangement with destructive interference in all but one diffraction order. This effectively channels all light into one single diffraction order. Finding an arrangement of the metaatoms that creates this interference is typically done numerically and is discussed in a later section. In **Fig. 3.9B**, a diffractive superunit cell is depicted with three metaatoms. Within this superunit cell, it is possible to alter the individual radii of the metaatoms ($r_1,\ r_2,\ r_3$), their height (h), and their relative positions ($g_1,\ g_2,\ g_3$). In addition, it has been theoretically shown that it is always possible to find an arrangement of the metaatoms in the superunit cell such that perfect destructive interference can be created, resulting in unity relative transmittance into the desired diffraction order [143]. However, this configuration does not necessarily correspond to a superunit cell that is practical to fabricate. In addition, it is possible to create a superunit cell metasurface with a one-dimensional superunit cell. In this one-dimensional unit cell the metaatoms are grating ridges that can be arranged to create the interference to channel light into one diffraction order. A metasurface constructed by the one-dimensional superunit cell are commonly referred to as metagratings.

Thus, the superunit cell functions as a local diffractive grating efficiently channeling light into one diffraction order. This implies that the local linear phase profile across the length of the superunit cell is determined

by the length of the diffractive period

$$\sin\left(\theta_{\mathrm{out,m}}\right) = \frac{\lambda}{n_{\mathrm{out}}}\frac{1}{a_{\mathrm{d}}}m. \tag{3.28}$$

Thus, the superunit cell can circumvent the spatial sampling rate in the phase-mapping approach, limited by the lattice constant (a), since it can produce an arbitrarily steep phase profile, instead determined by the diffractive periodicity (a_{d}). In **Fig. 3.10A**, the diffractive periodicity is presented as a function of the produced deflection angle of the local diffractive grating for transmission into air ($n = 1$) and a glass medium ($n = 1.51$). However, because the unit-cell length is inversely proportional to the phase profile across the superunit cell, the limitation for approximating a phase profile is reversed compared with the phase-mapping approach. When small-angle deflection is needed, the diffractive periodicity becomes large and provides poor resolution for approximating a desired phase profile. In addition, the large diffractive periodicity means that several diffraction orders will be opened (**Eq. 3.27**), which can require more metaatoms within each superunit cell to find an arrangement that creates constructive interference for only one desired diffraction order. With additional metaatoms and a larger superunit cell, the optimization problem of finding the optimal arrangement of metaatoms within the superunit cell becomes more computationally heavy to solve.

3.3.1 Phase profile for the superunit cell metasurfaces

Blazed grating

A basic application of the superunit cell is a blazed grating. Since the local phase profile is linear across the superunit cell, the phase profile of a blazed grating can be created by keeping the periodicity (a_{d}) constant across the entire metasurface. Although basic, the superunit cell can deflect light to very steep angles with exceptional efficiency.

Superunit cell metalenses

To focus light, the periodicity of the phase profile must decrease radially, leading to rapid changes in the phase profile, as seen from **Eq. 3.2** and **Fig. 3.2A**. As discussed, the phase-mapping approach cannot adequately resolve the phase profile when it changes too rapidly. As a result,

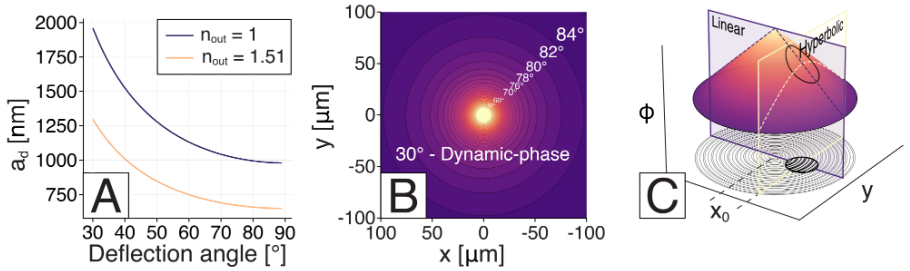

Figure 3.10: A) The diffractive period of the superunit cell (a_d) as a function of the Deflection angle when light is diffracted into air ($n_\mathrm{out} = 1$) or a glass medium ($n_\mathrm{out} = 1.51$). **B)** The annular deflection zones for creating a superunit cell metalens, discretized in steps of 2°. For smaller deflection angles, the diffractive periodicity becomes very large. However, it is possible to switch to the phase-mapping approach when smaller angles ($< 30°$) are required for the phase profile [144]. **C)** By turning the superunit cells into concentric circles, the radially linear phase profile of an axicon is achieved. By offsetting the axicon, the phase profile is linear in one dimension (deflection) and hyperbolic in the other (focusing), as visualized by planes cutting the cone along either axis.

with a fixed lattice constant in the phase-mapping approach, the phase profile is not well approximated at the periphery of a metalens. To instead construct the superunit cell metalens, the lens is discretized into distinct annular zones, or Fresnel zones, each assigned a diffractive periodicity to deflect light to a common focal point. To create a superunit cell metalens with focal length f, the local diffractive periodicity ($a_\mathrm{d}(r)$) in an annular zone at radius (r) can be found by trigonometry as

$$a_\mathrm{d}(r) = \frac{\lambda}{n_\mathrm{out}} \frac{\sqrt{r^2 + f^2}}{r}. \tag{3.29}$$

In **Fig. 3.10B**, the required deflection angle for a superunit cell metalens with focal length $f = 12$ µm can be seen when the annular zones are discretized in 2° steps. As mentioned, a small deflection angle corresponds to a large superunit cell periodicity, which is computationally inefficient and has poor resolution[6]. However, it has been demonstrated that it is possible to combine the best of both approaches [144], with phase mapping in the middle of the lens for the lower deflection angles

[6] At the very center of the lens, the beam is supposed to be deflected by $\Theta = 0°$, which corresponds to an infinite diffractive periodicity (a_d). This is hard to fabricate.

($\theta < 30°$) and then switching to superunit cells at the periphery of the metalens when large angles are needed, as shown in **Fig. 3.10B**.

Superunit cell axicon

Another possibility for beam shaping with a superunit cell metasurface is to create the phase profile of an axicon. If superunit cells with the same diffractive periodicity (a_d) are arranged in concentric circles to deflect light towards the center, the resulting phase profile becomes radially linear. This is exactly the phase profile of an axicon, from **Eq. 3.2** and as seen in **Fig. 3.2C**, and repeated here

$$\phi_\mathrm{axicon} = -\frac{2\pi n_\mathrm{out}}{\lambda}\mathrm{NA}\sqrt{x^2+y^2} \tag{3.30}$$

where n_out is the refractive index of the medium for the transmitted beam, and NA is the numerical aperture of the axicon. The radially linear (conic) phase profile creates two counter-propagating beams, generating a non-diffractive Bessel beam if the axicon is centered on the incident beam.

However, if the axicon phase profile is shifted off-center (x_0), the imparted phase profile now becomes linear along the x-axis and hyperbolic along the y-axis, as illustrated by the planes intersecting the conical phase profile in **Fig. 3.10C**. The linear phase profile can deflect the beam to a steep deflection angle via the diffractive periodicity (a_d). Because the phase profile is linear, the incident beam retains its divergence along the x-axis. Along the y-axis, the light is instead focused via the hyperbolic profile. The slope of this hyperbolic profile depends on how far the phase profile is shifted along the x-axis. Thus, this shift (x_0) can be used to determine a specific focal length along the y-axis. The phase profile of an axicon (**Fig. 3.10C**) shifted by an offset (x_0) along the x-axis is

$$\phi_\mathrm{offset} = -\frac{2\pi n_\mathrm{out}}{\lambda}\mathrm{NA}\sqrt{(x-x_0)^2+y^2}. \tag{3.31}$$

To find the focal length, this phase profile is compared to the phase profile of a lens from **Eq. 3.2** [145]. By changing the offset (x_0) such that the offset-axicon phase profile (ϕ_offset) matches ($\Delta\phi \to 0$) the lens phase profile (ϕ_lens) along the y-axis gives the corresponding focal length

$$\begin{aligned}\Delta\phi &= \phi_\mathrm{lens} - \phi_\mathrm{offset} \to 0 \\ &= n_\mathrm{out}\mathrm{NA}\sqrt{x_0^2+y^2} - n_\mathrm{out}\left(\sqrt{y^2-f^2}-f\right) \to 0.\end{aligned} \tag{3.32}$$

Furthermore, the illustration in **Fig. 3.10C** shows the concentric circles formed by the superunit cells beneath the conical phase profile. When cutting out a circle of the phase profile to be implemented within a practical metasurface with a certain diameter, the offset (x_0) corresponds to a certain curvature of the superunit cells.

3.4 Metasurface simulations

Once the phase profile and metaatom geometry that can fulfill the desired beam shaping are determined, the next step is to find the exact metaatom dimensions that can be used to approximate the desired optical response ($\mathbf{J}(x, y)$). The most common approach is to numerically solve the metaatom response using full-wave simulations. However, a final metasurface comprises hundreds of thousands to several million metaatoms[7], a scale that is not feasible to simulate with full-wave methods. However, the optical response of an individual metaatom can be approximated by utilizing periodic boundary conditions. Several numerical schemes aim to compute the response of a metasurface as efficiently and accurately as possible [146–148].

3.4.1 Individual metaatoms with periodic boundaries

A simulation of an individual metaatom is exemplified in **Fig. 3.11A** by a cylindrical GaAs metaatom ($n_{\mathrm{GaAs}} = 3.52$)[8] on a GaAs substrate with an air environment ($n = 1$). The metaatom is shown, along with the resulting distribution of the electric field under plane-wave excitation (E_{in}) from the substrate side at the wavelength $\lambda_0 = 980$ nm. As discussed earlier, a cylinder is a suitable geometry for approximating the phase profile with a dynamic-phase metasurface, where the height (h) and radius (r) can be varied to achieve different local transmittance ($|\hat{j}|$) and phase delays (ϕ). A parametric sweep of the GaAs cylinder is illustrated in **Fig. 3.11B-C** for the local transmittance and phase delay as a function of the radius (r) and height (h) of the cylindrical

[7]For instance, the metasurfaces fabricated for this thesis, with a unit-cell periodicity of $a = 260$ nm and a diameter of $d = 200$ µm, consist of over 400,000 individual metaatoms. In perspective, a standard desktop computer can handle full-wave simulations for tens to hundreds of unit cells.

[8]The refractive index of GaAs at $\lambda_0 = 980$ nm [149]. The designed lasing wavelength of the GaAs-VCSELs.

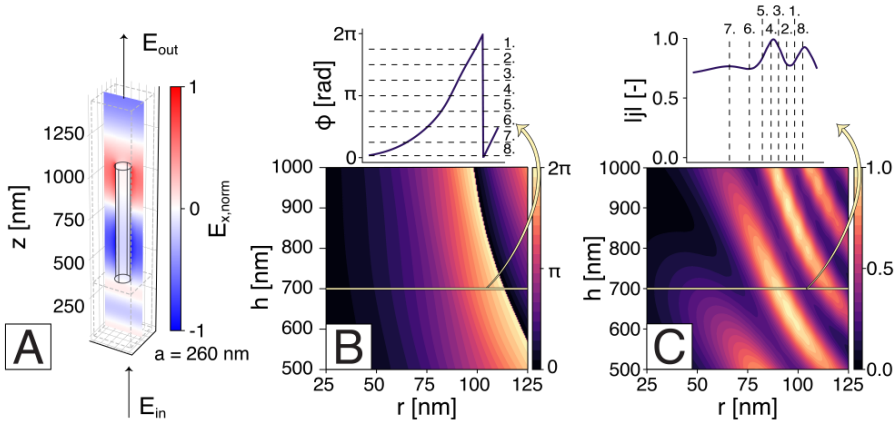

Figure 3.11: **A)** The simulated electric field (E_x) for a cylindrical GaAs metaatom with periodic boundary conditions under plane-wave excitation from the substrate side. **B)** The corresponding phase delays (ϕ) of the metaatom as a function of the radius (r) and the height (h). Inset: Discrete phase delays for metaatoms with height $h = 700$ nm when discretizing the 0–2π range in eight equal steps. **C)** Similarly, the transmission ($|\hat{j}|$) of the cylindrical metaatoms. Inset: The transmission for the eight metaatoms with height $h = 700$ nm that are evenly discretizing the 0–2π range.

GaAs metaatom. From these maps, a set of metaatoms can now be selected to sample a phase profile (0–2π). For example, the insets in **Fig. 3.11B-C** show the discrete transmittance ($|\hat{j}|$) and phase delays (ϕ) for eight metaatoms with the constant height of $h = 700$ nm, evenly discretizing 0–2π in eight steps.

However, the simulations with periodic boundary conditions assume that the metaatom sits in an infinite lattice of identical metaatoms. In a fabricated metasurface, several (or most) metaatoms neighbor a metaatom with a different geometry, which is not accounted for in simulations with periodic boundary conditions. However, interactions between different metaatoms are argued to be small for high-contrast dielectric metaatoms, since the high-index metaatom typically sits in a lower-refractive-index environment, such as air. This confines the electric field within the metaatom at the center of the unit cell and limits the interaction to the neighboring unit cells.

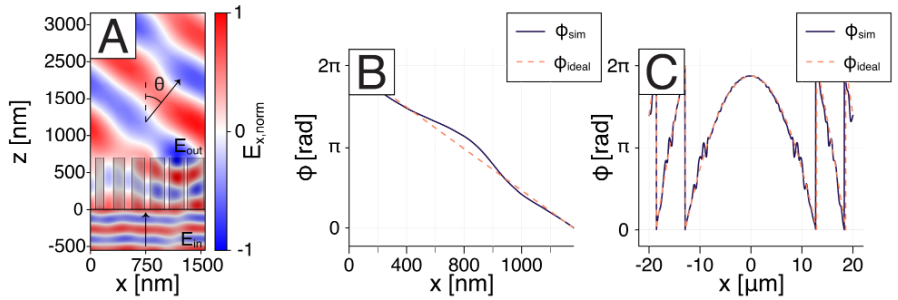

Figure 3.12: A) A slice of the electric field (E_x) for a blazed grating simulated with periodic boundary conditions. After propagating through the metaatoms, the electric field shows a clear oblique wavefront, corresponding to the designed deflection of the blazed grating. **B)** The extracted phase profile of the transmitted electric field (ϕ_{sim}) from a blazed grating simulation compared to the ideal linear phase profile (ϕ_{ideal}). **C)** The extracted phase profile from the transmitted electric field (ϕ_{sim}) for a cylindrical lens in a full-wave simulation compared to the ideal phase profile (ϕ_{ideal}).

Deflectors and cylindrical lenses

Although it is computationally infeasible to simulate the full-wave response of a full metasurface, the periodic boundary conditions can be utilized to find the full-wave response for at least two metasurfaces: a blazed grating and a cylindrical lens. These simulations allow extraction and verification of the phase profiles produced by a selected set of metaatoms from the parametric sweeping. To simulate a blazed grating, a set of metaatoms spanning 0 to 2π phase shift is arranged along one dimension to form the unit cell of the blazed grating, with periodic boundary conditions applied to the outer edges. The unit cell of the blazed grating is shown in **Fig. 3.12A**, with six cylindrical metaatoms evenly discretizing the 0–2π range, using the cylinders from the parametric sweep in **Fig. 3.11** with height $h = 700$ nm. Under illumination by a normally incident plane wave from the substrate side (E_{in}, $\lambda = 980$ nm), the blazed grating generates an oblique wavefront (E_{out}) propagating at a deflection angle ($\Theta_x = 38.92°$) corresponding to the length of the cell size (1560 nm)[9]. The imperfect wavefronts result

[9] If you think that this looks exactly like a superunit cell described in the previous section, you are correct. However, the placement and the sizes of the six metaatoms with this phase-mapping approach are not necessarily the most efficient solution for this superunit cell.

from non-uniform transmission of the metaatoms (**Fig. 3.11C**) and discretization of the phase profile. In **Fig. 3.12B**, the phase extracted from the transmitted beam (E_{out}) is compared with the ideal linear phase profile, demonstrating how well the discrete metaatoms can approximate the desired linear profile.

Similarly, a cylindrical lens can be simulated by arranging metaatoms to impart a hyperbolic phase profile along a single axis[10]. The unit cell of the cylindrical lens is again surrounded by periodic boundary conditions, which model an infinite, periodic array of cylindrical lenses. In **Fig. 3.12C**, the extracted phase profile for a cylindrical lens $f = 90$ µm, created with the cylindrical metaatoms from **Fig. 3.11**, discretizing the 0–2π range in eight even steps with the eight marked metaatoms in the figure. Under plane-wave excitation from the substrate side, the extracted phase profile aligns well with the ideal phase profile, as seen in **Fig. 3.12C**, with only some minor deviations occurring near the π-phase delays.

3.4.2 Superunit cell simulations

The superunit cell simulations are performed similarly to those for an individual metaatom, with periodic boundary conditions and plane-wave excitation from the substrate side. Schematically shown in **Fig. 3.13A** is the superunit cell of a metagrating, a one-dimensional superunit cell, with a diffractive period (a_{d}) large enough that diffraction orders are opened in transmission. The metagrating can be optimized to efficiently channel all light into one diffraction order by arranging the metaatoms, in this case ridges, within the superunit cell. For the metagrating, the parameters that can be optimized are the position of the grating grooves (g_1, g_2, g_3), the groove height (h), and the groove width (w). A major advantage of the superunit cell design for fabrication without an etch stop-layer is that it enables efficient deflection of light to steep angles while constraining the metagrating to grooves of uniform width (w).

The optimization goal is to find an arrangement of meta-atoms that maximizes both the overall transmission (η_t) and the relative transmission

[10] The phase profile of a cylindrical lens is a hyperbolic profile in one-dimension as $\phi_{\text{cyl}}(x) = \phi_{\text{lens}}(x, 0) = -\frac{2\pi n_{\text{out}}}{\lambda_0}\left(\sqrt{x^2 - f^2} - f\right)$.

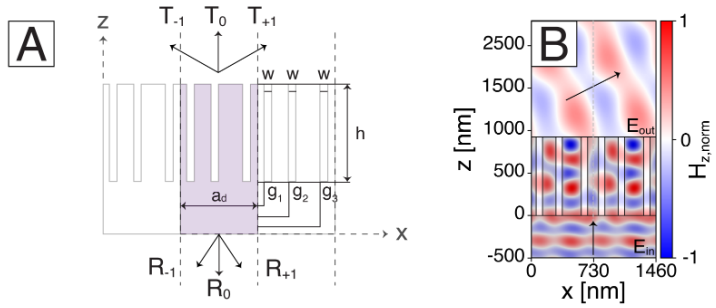

Figure 3.13: A) The superunit cell of the metagrating. Within the one-dimensional unit cell with diffractive periodicity a_{d}, the relative position (g_1, g_2, and g_3), the height (h), and the width (w) of the grating grooves can be optimized to find a solution with a large total (η_t) and relative (η_r) transmission efficiency into one diffraction order. **A)** The resulting magnetic field distribution ($H_{z,norm}$) can be seen for one such optimized solution, where a clear oblique wavefront can be seen after propagating away from the superunit cell at an angle of $\Theta_x = 62.75°$. Note in the figure there is two superunit cells, and the transmitted environment is glass ($n = 1.51$)

into the desired diffraction order (η_r), formulated as

$$\eta_t = \frac{\Sigma T_i}{\Sigma R_i}, \quad \eta_r = \frac{T_{+1}}{\Sigma T_i}. \tag{3.33}$$

In **Fig. 3.13B** the resulting magnetic field distribution ($H_{\mathrm{z,norm}}$) for one such optimized solution is shown, demonstrating a clear oblique wavefront after the superunit cell. The substrate in the simulation is GaAs ($n = 3.52$), which is sitting in a glass environment ($n = 1.51$). The diffractive periodicity ($a_{\mathrm{d}} = 730$ nm) that sets the deflection angle ($\Theta_x = 62.75°$). Something to keep in mind for the superunit cell simulations is that multiple diffraction orders are now open in both transmission and reflection (**Eq. 3.27**). To avoid spurious results, the boundary conditions in the numerical scheme must properly account for all propagating diffraction orders.

3.4.3 Metaatom simulation with FEM

All the individual metaatoms and the superunit cell are simulated using the finite element method (FEM) solver in the commercial software COMSOL Multiphysics [150]. While such commercial solvers are

assumed to compute Maxwell's equations reliably, the computational model must be properly configured to ensure the numerical solution converges to the true optical response [151]. This requires evaluation of the discretization (the mesh) and the boundary conditions used. For the mesh, any extracted parameters should asymptotically converge towards the true value as the mesh elements are refined. As an example, the phase delay (ϕ) for a birefringent half-waveplate is presented in **Fig. 3.14A** as a function of the mesh size parameter

$$L_{\text{min}} = \frac{1}{c_{\text{mesh}}} \frac{\lambda_0}{n}. \tag{3.34}$$

The mesh parameter (c_{mesh}) determines how many times the minimum element length (L_{min}) divides the local wavelength ($\frac{\lambda_0}{n}$). A rule of thumb for three-dimensional FEM simulations is that an element size of one-eighth of the effective wavelength should give a converging solution [150]. By assuming that the simulated model is converging to the true phase delay (ϕ_0) with an infinitesimal element size ($c_{\text{mesh}} \to \infty$), the order of convergence (α) and error for a certain element size can be found by fitting the exponential function

$$f(c_{\text{mesh}}) = \phi_0 + \phi_\alpha c_{\text{mesh}}^{-\alpha}. \tag{3.35}$$

By comparing the computed value for any mesh size to the true phase delay with the infinitesimal element length (ϕ_0), the relative error can be estimated for a certain mesh size as

$$e(c_{\text{mesh}}) = \log_{10} \left| \frac{\phi_{\text{sim}}(c_{\text{mesh}}) - \phi_0}{\phi_0} \right|. \tag{3.36}$$

The simulated relative error for the birefringent half-waveplate as a function of the mesh parameter (c_{mesh}) is shown in the inset of **Fig. 3.14A**. The same procedure applies to any extracted parameter. In addition, the mesh should be constructed first for higher-refractive-index domains in the simulation model, as this ensures the smaller elements of the dense medium are not constrained by the coarser mesh of the low-index domain.

For simulations with periodic boundary conditions, the mesh on opposite boundaries must be identical to enforce the periodic continuity of the fields. In addition, the placement of the excitation sources and extraction boundaries must be carefully considered to avoid interfering with

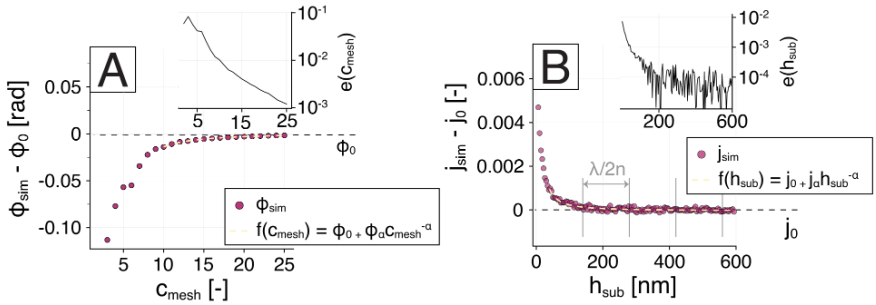

Figure 3.14: A) The simulated phase delay (ϕ) as the mesh of the simulation is refined (c_{mesh}). Inset: The relative error in the simulations as a function of the mesh parameter (c_{mesh}). **B)** The transmission ($\hat{j}_{\text{sim}}$) as the length of the substrate to the excitation port increases (h_{sub}). Inset: The error in the simulation as a function of the length of the substrate to the excitation port increases (h_{sub}).

the near-field scattering of the metaatoms. Another rule of thumb is to place the port at least half a wavelength in the port medium away ($\frac{\lambda_0}{2n}$). However, this can be checked by moving the boundaries away from the simulated metaatom. In **Fig. 3.14B**, the convergence of the transmittance as a function of the height of the substrate beneath the metaatoms is shown. In COMSOL, metaatoms are excited via periodic ports that implement a Robin boundary condition, allowing the incident field to be launched and the reflected or transmitted waves to be completely extracted. If these ports are placed too close to the metaatom, near-field evanescent waves spuriously couple into the Robin boundary condition. This is the reason for the larger transmittance seen when the substrate height is smaller than half a wavelength in the substrate ($h_{\text{sub}} < \frac{\lambda_0}{2n}$), as seen in **Fig. 3.14B**.

3.5 Metasurface fabrication

3.5.1 Process flow for GaAs metasurfaces

The major advantage of metasurfaces is the ability to pattern the entire optical component in a single lithographic step. The GaAs etch recipe was optimized to achieve the highest possible aspect ratio while maintaining vertical sidewalls. To accomplish this, the procedure uses a switched etching process [145], conceptually similar to the Bosch process used for deep reactive-ion etching of silicon, where etching is cycled

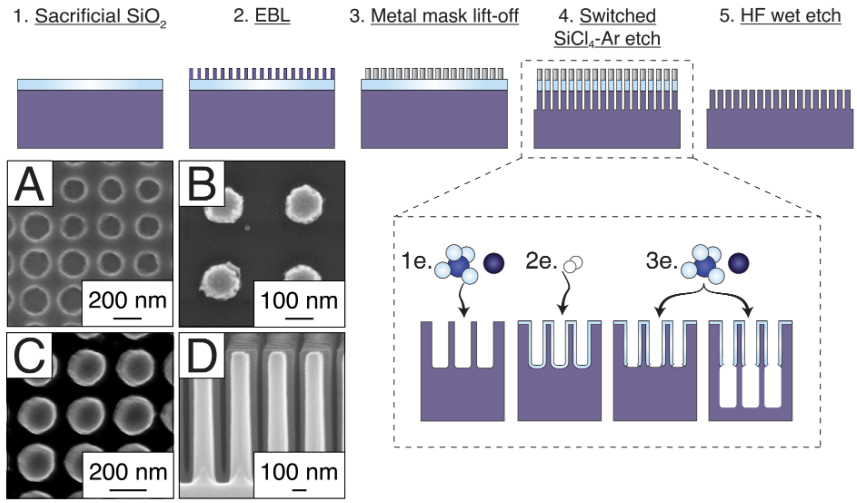

Figure 3.15: The GaAs metasurface process with the switched $SiCl_4$–Ar etch highlighted. The SEM images show the major processing steps. **B)** Top view of the developed resist (step 2). **B)** Top view of the Ni/Cr metal mask after lift-off (step 3). **C)** Top view of etched metaatoms (step 4). **D)** Cross-section of the etched metaatoms after the HF wet etch (step 5).

between an etching step and a sidewall passivation step. In addition, the etching process utilizes a metal hard mask for dry etching to provide high etch selectivity between the mask and GaAs. The complete process flow is presented in **Fig. 3.15** and summarized as follows:

1. **Sacrificial SiO_2 :** Deposition of a sputtered 25–50 nm-thick layer of SiO_2 to act as a sacrificial layer to later lift off the metal hard mask.

2. **Electron beam lithography:** The samples are baked at 160°C and primed with hexamethyldisilazane (HMDS) to prepare the surface. The positive-tone resist AR-P6200 (diluted 1:1) is spin-coated at 4500 rpm, resulting in a 120 nm-thick film, and exposed with a dose ranging from 180–240 $\mu C/cm^2$ depending on the density of the metasurface pattern. The resist is developed in hydrophobic n-amyl acetate for 90 s and rinsed with isopropyl alcohol (IPA).

3. **Metal mask lift-off:** A 10/50 nm Cr/Ni stack is deposited via electron-beam evaporation. The thin Cr provides adhesion to the

SiO_2, and Ni provides high etching selectivity. The sample is then submerged in mr-Rem 400 to dissolve the resist and lift off the metal. Because the metasurface fabrication takes place on the substrate side of the fully processed VCSEL, ultrasonic cleaning for the lift-off is not possible. The small VCSEL mesa (20–25 µm), with small oxide apertures, can easily be damaged by the acoustic cavitation. Instead, a spray gun loaded with acetone is used to clean the metal mask from the sample.

4. **Switched $SiCl_4$–Ar etch:** The sacrificial SiO_2 layer is first dry-etched using a CF_4 RIE. The anisotropic GaAs etch is then performed by switching between $SiCl_4$–Ar etching steps (8/42 sccm, 25–35 s) and O_2–Ar sidewall passivation steps (2/48 sccm, 5 s), intermediated with an Ar purging step (50 sccm, 5 s). The cyclic process is highlighted in **Fig. 3.15** and proceeds as follows: (**1e.**) The $SiCl_4$–Ar plasma anisotropically etches the GaAs. (**2e.**) The chamber is flushed with O_2, which reacts with residual Si to form a passivating SiO_2 film. (**3e.**) In the subsequent etching cycle, directional ion bombardment clears this passivation film from the horizontal surfaces, leaving the passivating SiO_2 film on the sidewalls. The $SiCl_4$–Ar etching step is performed with 30 W platen power, 25 W ICP power, and a chamber pressure of 1.7–2.0 mT.

5. **HF wet etch:** The metal etching mask is released by wet etching the sacrificial SiO_2 layer with hydrofluoric acid (HF). The substrate is continuously agitated during this step to prevent the released metal film from electrostatically re-adhering, leaving a pristine GaAs metasurface.

3.5.2 Aspect-ratio dependent etching

An inherent challenge when etching without a defined stop layer is that larger gaps in the pattern are etched deeper than smaller ones, a phenomenon known as aspect-ratio-dependent etching (ARDE). In **Fig. 3.16A**, the etch rate per cycle of the switched process is presented as a function of the aspect ratio of the etched calibration gratings. A cross-section of one such calibration grating is shown in **Fig. 3.16B**, together with the ARDE effect observed when etching cylinders for a dynamic-phase metasurface in **Fig. 3.16C**. One approach to mitigate ARDE is to characterize the etch-rate dependence across gap sizes and

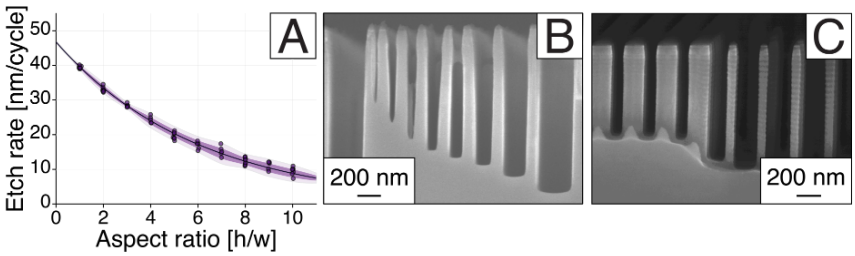

Figure 3.16: A) Etch rate per cycle of the switched GaAs etching as a function of the aspect ratio of etched grating lines. **B)** Cross-section of etched grating bars with a range of gaps (w = 10–200 nm), which shows the ARDE effect from etching without a stop layer. **C)** Cross-section of etched cylindrical metaatoms (r = 25, 95 nm). The scallops seen on the cylinders are due to the switched etching process.

then compensate for the depth variation in the design process. An alternative is to constrain the metasurface pattern to uniformly sized gaps, ensuring a constant etch depth over the entire metasurface and circumventing ARDE. This second approach is a major advantage for designing metasurfaces with superunit cell designs, as it is possible to optimize highly efficient superunit cells with only uniform gaps, which automatically ensures an even etch depth across the whole metasurface.

3.6 Transmission characterization of metasurfaces

The objective of characterizing a fabricated metasurface before VCSEL integration is to verify the imparted phase profiles and relative transmission efficiency. I rely on Fourier imaging of the transmitted beam ($\mathbf{E}_{\text{out}}$), using the setup illustrated in **Fig. 3.17A**. When an infinity-corrected objective is focused on the metasurface plane, it separates the field into its constituent plane waves (spatial frequencies or in-plane momenta) at its back focal plane. In a standard microscope, a tube lens reassembles these plane waves into a real-space image, which can be captured by a charge-coupled device (CCD) camera. However, introducing another lens (a Bertrand lens) changes the image projected onto the camera. By focusing the Bertrand lens on the back focal plane of the objective, the plane-wave spectrum ($\mathcal{F}[E_{\text{out}}]$) itself is projected onto the CCD camera.

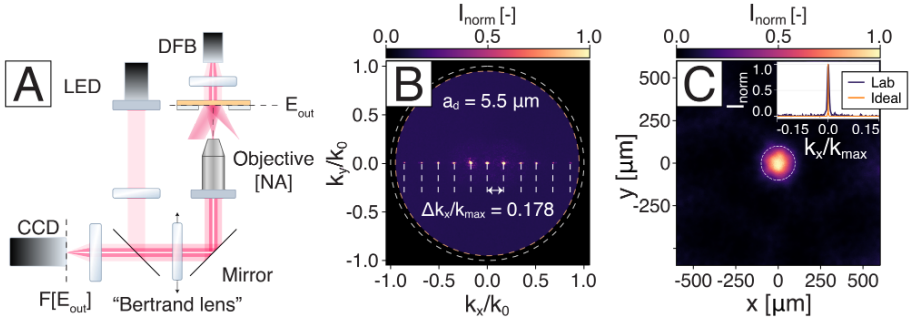

Figure 3.17: **A)** Experimental setup for Fourier-plane imaging, where a Bertrand lens enables the CCD to capture the plane-wave spectrum ($\mathcal{F}[E_{\text{out}}]$). **B)** Calibration of the plane-wave spectrum using a calibration grating ($a_{\text{d}} = 5.5\,\mu\text{m}$). **C)** The loosely collimated Gaussian illumination beam ($w_0 = 100\,\mu\text{m}$ at $1/e^2$). Inset: Measured line profile of the plane-wave spectrum of the loosely collimated Gaussian beam compared against an ideal Gaussian beam of equal width.

When imaging the plane-wave spectrum, the spatial position (r) of the light on the CCD maps to a plane wave with an in-plane deflection angle ($\Theta_\perp$) or in-plane wave vector ($k_\perp$) as

$$r = n f_{\text{eff}} \sin\Theta_\perp = f_{\text{eff}} \frac{k_\perp}{k_0}, \tag{3.37}$$

where n is the refractive index of the imaged medium, f_{eff} is the effective focal length of the entire imaging system, accounting for the objective, the Bertrand lens, the tube lens, and any additional optics. Although the mapping from the position on the CCD camera can be analytically determined from **Eq. 3.37**, it is arguably simpler to calibrate the acquired image using a known structure. In **Fig. 3.17B**, a Fourier image is presented where a grating with a known periodicity ($a_{\text{d}} = 5.5\,\mu\text{m}$) is illuminated by a loosely focused Gaussian beam, collected by an objective with a numerical aperture NA $= 0.95$. With a wavelength of the illuminating laser at $\lambda_0 = 980$ nm, this yields a deflection angle of $\Theta = 10.26°$ between the diffraction orders. This corresponds to an offset of $k_\perp/k_0 = 0.178$ in the plane-wave spectrum, which is used to map the sensor positions to the plane-wave components. Furthermore, the largest plane-wave angle that can be captured will be limited by the numerical aperture of the imaging objective used

$$\text{NA} = n_{\text{obj}} \sin\Theta_{\text{max}}, \tag{3.38}$$

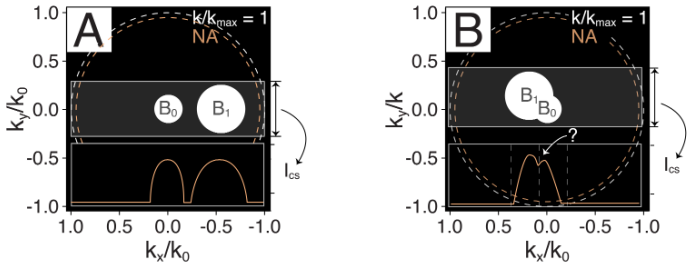

Figure 3.18: A) A fictional plane-wave spectrum when illuminating a metasurface, where two distinct beams are visible. The zero-order beam, B_0, corresponds to the untransformed light from a normally incident source that has not acquired a phase profile from the metasurface. The other beam, B_1, represents light that has acquired a phase profile with a shifted and broadened plane-wave spectrum. **B)** When the phase profile of the metasurface does not spatially separate the transformed light (B_1) from the light in the zero-order beam (B_0), it becomes difficult to fairly estimate the relative transmission efficiency (η_r).

where n_{obj} is the refractive index of the image medium, and Θ_{max} is the maximum acceptance angle. In addition, to characterize the plane-wave spectrum of the fabricated metasurfaces, they are illuminated with a loosely focused Gaussian beam. In **Fig. 3.17C**, an image of the loosely focused beam (w_0 =100 µm) used to illuminate the metasurfaces is shown, with an inset that compares the plane-wave spectrum to an ideal Gaussian beam with the same width.

The imparted phase profile can be evaluated by comparing the acquired plane-wave spectrum to the Fourier transform of a numerically calculated electric field ($\mathcal{F}[E_{\text{out}}]$). Two fictional examples of plane-wave spectra are illustrated in **Fig. 3.18**. The white dashed line marks the limit of the plane-wave spectrum ($k/k_0 = 1$), which corresponds to a plane wave with the in-plane propagation angle of 90°. The yellow dashed line indicates the NA of the imaging objective (**Eq. 3.38**). Since the imaging objective cannot collect plane waves with angles larger than the NA, the region outside the NA is dark in all the following Fourier images. All Fourier images are plotted on a logarithmic scale and normalized to peak pixel intensity, with I_{cs} denoting the integrated intensity for the marked cross-section.

The example in **Fig. 3.18A** illustrates two distinct beams in the plane-wave spectrum. Because practical metasurfaces seldom achieve 100% conversion efficiency, a fraction of the incident light does not acquire the designed phase profile and retains its original plane-wave distribution. Under normal incidence (**Fig. 3.17**), this untransformed light is centered at $k/k_0 = 0$ and is denoted as the zero-order beam (B_0). In contrast, beam one (B_1) represents the light that acquires the phase profile of the metasurface. Its shift in momentum space confirms that the metasurface deflects the incident beam by an angle Θ, while the spectral broadening of the beam indicates a focusing effect. A peculiarity of Fourier imaging is that it records only the angular spectrum. Therefore, it cannot distinguish whether a beam is converging or diverging in the real-space image plane, as both cases correspond to the same plane-wave spectra. The relative transmission efficiency (η_r) of the fabricated metasurfaces is estimated by integrating the captured intensity in the Fourier images, comparing the integrated power of the transformed beam (B_1) to that of the untransformed zero-order beam (B_0). However, this estimation can be challenging when the respective plane-wave spectra are difficult to isolate. This limitation is exemplified in **Fig. 3.18B**, where significant spatial overlap between B_0 and B_1 makes it difficult to draw a fair integration boundary to separate the two beams.

3.6.1 Stokes parameters

For metasurface designs that use birefringent metaatoms, the polarization state of the incident beam transforms due to the interaction with the metasurface. To capture the polarization states, we have used Stokes polarimetry with the rotating quarter-waveplate (QWP) technique. The experimental setup is schematically shown in **Fig. 3.19A** for the rotating QWP technique, where the rotation ($\theta_{\lambda/4}$) of a QWP followed by a fixed linear polarizer can be used to extract the Stokes vector [152], defined here as

$$\begin{aligned} S &= [S_0, S_1, S_2, S_3] \\ S_0 &= E_x^2 + E_y^2 \\ S_1 &= E_x^2 - E_y^2 \\ S_2 &= 2E_xE_y\cos\delta \\ S_3 &= 2E_xE_y\sin\delta, \quad \delta = \phi_y - \phi_x. \end{aligned} \tag{3.39}$$

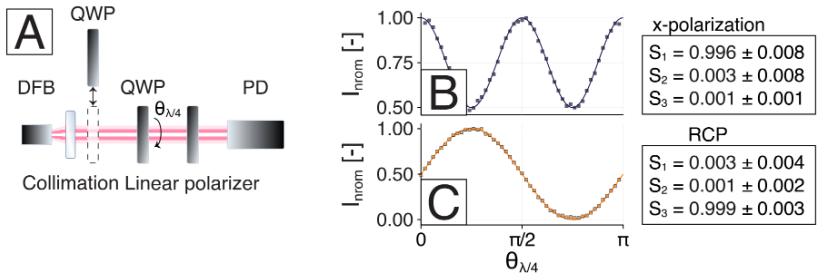

Figure 3.19: A) Experimental setup for Stokes polarimetry with the rotating QWP technique. **B)** The recorded intensity as a function of the angle of the QWP ($\theta_{\lambda/4}$) together with the Fourier series from **Eq. 3.41** for a linearly polarized state emitted by the distributed-feedback (DFB) laser. **C)** Similarly, the recorded intensity as a function of the angle of the QWP ($\theta_{\lambda/4}$) when the QWP converts the linear polarization state of the DFB laser into an RCP state.

These parameters fully describe the polarization state of light and are typically represented geometrically on a sphere ($S_0^2 = S_1^2 + S_2^2 + S_3^2$), known as the Poincaré sphere[11]. For the rotating QWP method, it can be shown with Jones calculus that the measured intensity after a QWP rotated by an angle ($\theta_{\lambda/4}$) and a linear polarizer is

$$I(\theta_{\lambda/4}) = \frac{1}{2}\left[S_0 + S_1\cos^2(2\theta_{\lambda/4}) + S_2\sin(2\theta_{\lambda/4})\cos(2\theta_{\lambda/4}) + S_3\sin(2\theta_{\lambda/4})\right]. \tag{3.40}$$

This can be rewritten into the truncated Fourier series

$$I(\theta_{\lambda/4}) = A + B\sin(2\theta_{\lambda/4}) + C\cos(4\theta_{\lambda/4}) + D\sin(4\theta_{\lambda/4}), \tag{3.41}$$

where the Stokes parameters are acquired by estimating the Fourier coefficients from several intensity measurements.

In **Fig. 3.19B-C**, the recorded intensities for the calibration measurement of the rotating QWP technique are shown for both the linear polarization state and the RCP state. Since no physical QWP is ideal for every wavelength, the actual phase retardation and attenuation at the measured wavelength must be accounted for. A detailed procedure for calibrating the measurements with non-ideal QWPs for the methodology

[11] Which can be seen in **Fig. 3.6C**, where it was used to visualize the geometric phase due to the polarization state conversion from the interaction with a half-waveplate nanofin.

above is described by Berry *et al.* [153]. Furthermore, the technique is sensitive to the accuracy of the QWP rotation angle ($\theta_{\lambda/4}$), an error that can be reduced by oversampling. In all presented Stokes measurements, I used at least 50 intensity measurements, reducing the standard deviation of the acquired Stokes parameters to $< 10^{-2}$, as shown in **Fig. 3.19B-C**, calculated from the average deviation of the recorded intensities.

3.6.2 Fabricated metasurfaces

The following are examples of the Fourier images of the fabricated metasurfaces, captured by a high-NA objective in air (NA = 0.95) and illuminated by the loosely collimated Gaussian beam (**Fig. 3.17**). The phase profiles used can be referenced from **Eq. 3.2**.

Figure 3.20A shows a geometric-phase metasurface designed to focus RCP light ($f = 178\,\mu m$) and deflect it by an angle ($\Theta_x = 20°$)[12]. If the focal length of $f = 178\,\mu m$ seems ad hoc, it is the focal length of a hyperbolic phase profile to collimate the emitted beam from the fabricated bottom-emitting VCSELs. The linearly polarized beam is split into its RCP and LCP constituents at the designed angle, as seen by the shift of the maximum of the two beams to $k_x/k_0 = \pm 0.34$, which corresponds to the designed deflection angle of $\Theta_x \pm 20°$. The spreading of the plane-wave spectrum of both beams corresponds to the hyperbolic phase profile imparted by the metasurface. As such, both RCP and LCP components spread in the plane-wave spectrum, corresponding to both converging and diverging beams, since the hyperbolic phase profile is imparted with opposite signs to the two states. The relative transmission efficiency is taken from the integrated areas shown in **Fig. 3.20A** and estimated to be $\eta_r = 79\%$. **Figure 3.20B** shows an SEM image of a tilted view of the border of the fabricated geometric-phase metasurface, and **Fig. 3.20C** shows a top view of the etched nanofins.

Similarly, **Fig. 3.20D** presents the Fourier image of an APM designed to focus light with the dynamic phase ($f = 178\,\mu m$) and split RCP and LCP components via the geometric phase by deflecting both states

[12]The nanofins of the metasurface have widths $w_x = 202$ nm, $w_y = 91$ nm, and a height $h = 1000$ nm. The complex transmission coefficients for this nanofin are shown in **Fig. 3.7D**.

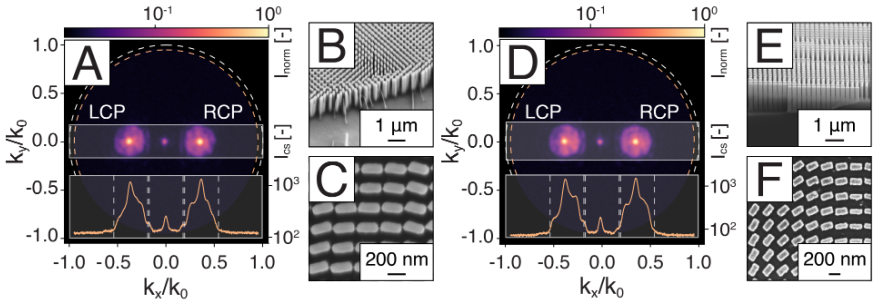

Figure 3.20: **A)** Fourier image of the fabricated geometric-phase metasurfaces, illuminated by a loosely focused Gaussian beam and captured with a high-NA objective (NA = 0.95). **B)** SEM image of a tilted view and **C)** a top view of the etched geometric-phase metasurface. **D)** Similarly, the Fourier image of the APM. **E)** SEM image of a cross-section of the metasurface and **F)** a top view of the metal Cr/Ni etching mask for the metasurface.

($\Theta = \pm 20°$)[13]. The Fourier image again shows the shift in the plane-wave spectrum for both polarization states, $k_x/k_0 \approx \pm 0.34$, and the spread of their respective plane-wave spectra now corresponds to both beams being focused by the dynamic phase of the APM. The relative transmission efficiency is estimated to be $\eta_r = 87\%$ from the marked areas in the figure. **Figure 3.20E** shows an SEM image of a cleaved cross-section of the APM, and **Fig. 3.20F** shows a top view of the etched metasurface.

In **Fig. 3.21A**, the Fourier image captured from an offset-axicon metagrating is presented. The diffractive periodicity ($a_\mathrm{d} = 1136$ nm) of the metagrating deflects the beam to the target deflection angle, $\Theta_x = 60°$, which corresponds to $k_x/k_0 = 0.866$ in the Fourier image[14]. The offset ($x_0 = 240$ µm **Eq. 3.32**) of the axicon spreads the plane-wave spectrum along the y-axis, where this particular offset is intended to collimate the beam from the bottom-emitting VCSEL along the y-axis. Because the metagrating uses only gaps of exactly the same width across the entire metasurface, ARDE is circumvented, resulting in a relative transmission efficiency estimated at $\eta_r = 87\%$.

[13]The nanofins for the APM are designed to discretize the dynamic phase into five discrete steps, with dimensions presented in **Fig. 3.7D**.

[14]The optimized grating parameters can be found in Juodėnas *et al.* [145]. Furthermore, it is not the most exciting Fourier image to look at, since it is mostly empty. However, the next chapter presents the produced fan-shaped beam in real space when this metasurface is monolithically integrated with the VCSEL.

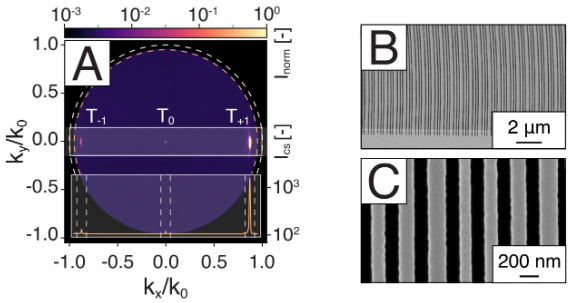

Figure 3.21: A) Fourier image of the fabricated offset-axicon metagratings with offset $x_0 = 240$ µm. **B)** SEM image of a tilted view of the cross-section of the fabricated curved grating and **C)** a top view of the etched grating.

The last example in **Fig. 3.22** is for a superunit cell metalens designed to deflect light by a steep angle according to **Eq. 3.29**. A metalens can simultaneously deflect and focus light by offsetting the phase profile. By trigonometry, the offset from the center (r_0) for a certain focal length (f) and deflection angle (Θ) is

$$r_0 = f \tan(\Theta). \tag{3.42}$$

Figure 3.22A shows the Fourier image of a superunit cell metalens designed with a focal length $f = 600$ µm and deflection angle $\Theta = 61°$. While the metasurface superunit cells efficiently channel the beam into the desired diffraction order ($\eta_r = 68\%$), achieving a small focus requires a much larger angular spread of deflection angles across the metasurface[15]. Because of the small size of the metasurface, it only covers a narrow range of deflection angles, $\Theta = 59°$–$62°$, which limits the minimum spot size. To examine the spot size, the deflected beam is also captured in real space. A cross-section of a captured z-stack for the beam is presented in **Fig. 3.22B**. The inset shows a line profile of the intensity at the designed focal plane, measuring a spot size of $d_{\text{spot}} = 16.6$ µm, taken as the $1/e^2$-width. Furthermore, **Fig. 3.22C** presents the map of the deflection angles across the fabricated metasurface, highlighting that the limited spatial extent of the metasurface imparts only five discrete angles to the incident beam. Decreasing the focal length (f) or increasing the metalens diameter would expand this angular range

[15] All the simulation data on the superunit cell metasurface can be found in the thesis *Large-angle deflection lens using supercell metasurfaces* [154].

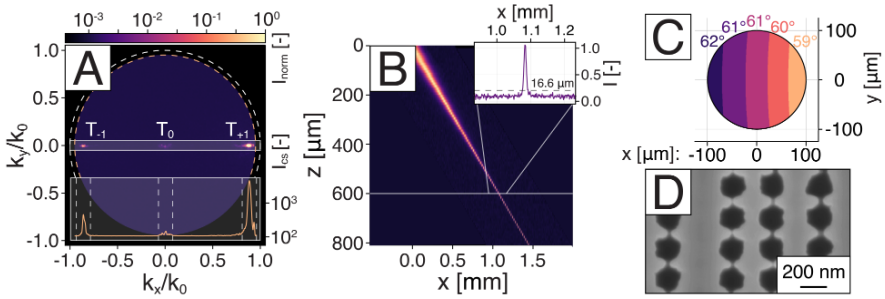

Figure 3.22: A) Fourier image of the fabricated superunit cell metalens. **B)** z-stack of the cross-section of the generated beam. Inset: the line profile at the designed focal plane ($L_\mathrm{f} = 600\,\mu\mathrm{m}$) with a spot size of $d_\mathrm{spot} = 16.6\,\mu\mathrm{m}$ measured from the $1/e^2$-width. **C)** Deflection angles and curvature of the fabricated superunit cell metalens. **D)** SEM image of the top view of the fabricated metalens with holes of the same size to circumvent ARDE.

(effectively increasing the numerical aperture), significantly reducing the spot size in the focal plane. Finally, **Figure 3.22D** shows a top-view SEM image of the superunit cell, which utilizes uniform hole diameters to circumvent ARDE. The imaged superunit cell has a diffractive periodicity of $a_\mathrm{d} = 1125$ nm for the deflection of light to $\Theta = 61°$, which is used as the central strip in **Fig. 3.22C**.